

# Experimental and theoretical study of ion distributions near 300 $\mu\text{m}$ tall steps on rf-biased wafers in high density plasmas

J. R. Woodworth,<sup>a)</sup> P. A. Miller, R. J. Shul, I. C. Abraham, B. P. Aragon,  
and T. W. Hamilton

*Sandia National Laboratories, Albuquerque, New Mexico 87185-1193*

C. G. Willison

*L & M Technologies, Albuquerque, New Mexico 87109-5802*

D. Kim and D. J. Economou

*Department of Chemical Engineering, Plasma Processing Laboratory, University of Houston, Houston, Texas 77204-4004*

(Received 13 March 2002; accepted 14 October 2002; published 9 December 2002)

We present an experimental and theoretical study of ion fluxes, energy distributions, and angular distributions close to 300  $\mu\text{m}$  tall “steps” on rf-biased wafers in high-density argon plasmas. This feature size is important in the etching of microelectromechanical systems. The theory and data show good agreement in most of the trends in the ion distributions as our sampling point approaches the foot of the step: (1) the ion flux decreases, (2) the ions move away from vertical, turning towards the step, and (3) the widths of the double-peaked ion energy distributions become narrower. The theory predicts that the hot neutral flux near the foot of the step is comparable to the ion flux. These hot neutrals may have important effects on the etching process. © 2003 American Vacuum Society. [DOI: 10.1116/1.1527951]

## I. INTRODUCTION

Inductively coupled plasma reactors are used for the etching of microelectromechanical systems (MEMS),<sup>1–3</sup> integrated circuits, and photonic circuits. Large feature sizes ( $\sim 300 \mu\text{m}$ ) are of particular interest to MEMS devices. In the inductively coupled discharges used to etch MEMS, a rf-coil couples energy through a dielectric window to excite a low pressure plasma. The wafer to be etched is placed on a chuck in direct contact with the plasma and is bombarded by ions and neutrals. A rf bias voltage is also usually applied to the chuck, influencing the energy of the ions striking the wafer.

In order to understand in detail the etching of devices on the MEMS scale, it is essential to have models tightly coupled to experimental data. While there are a variety of models available for both the bulk plasmas,<sup>4–11</sup> and etching in small features,<sup>12,13</sup> there is a scarcity of data to compare to these models. A number of authors have measured ion energy distributions at grounded surfaces<sup>14–22</sup> or at rf-biased electrodes in low density discharges.<sup>23–28</sup> A few authors have reported ion energy distribution measurements at rf biased electrodes in inductively driven discharges,<sup>29–34</sup> but only on flat surfaces.

In all of the above studies, the plasma was in contact with a planar substrate and the sheath over that substrate was one dimensional. There are several applications, however (including plasma source ion implantation, neutral beam processing, plasma thrusters, and the fabrication of MEMS), for which the size of features on the substrate can be comparable to or larger than the sheath thickness. The plasma would then

try to “mold” over the surface topography, i.e., the plasma–sheath boundary or meniscus would not be planar anymore. The resulting curved electric field lines can alter the oncoming ion trajectories, greatly influencing the ion angular distributions (IADs). The ion flux and ion energy distributions (IEDs) along the surface contour can also be affected.

Very little experimental work has been done on structured (nonplanar) wafer surfaces. We have previously reported ion energy distributions near  $\sim 3\text{-mm}$  tall steps on grounded electrodes<sup>35</sup> and inside 100  $\mu\text{m}$  square holes<sup>36</sup> on an rf-biased wafer. We report here on measurements of ion energy and angular distributions near  $\sim 300 \mu\text{m}$  tall steps on a rf-biased wafer in an inductively driven discharge and compare these measurements to the results of fluid and Monte Carlo simulations. Since the steps present a two-dimensional (2D) problem, we are able to compare the data from these experiments directly to 2D model predictions.

## II. APPARATUS

### A. Discharge cell

Our experiments were carried out using pure argon discharges in a gaseous electronics conference reference cell (GEC Ref Cell)<sup>37</sup> which had been modified to produce inductively driven discharges.<sup>38</sup> Figure 1 shows a schematic of our GEC Ref Cell, which has been described in detail previously.<sup>32,36</sup> A Faraday shield between the rf entrance window and the 13.56 MHz induction coil minimized capacitive coupling between the induction coil and the plasma. The wafer chuck was driven capacitively by a separate 13.56 MHz power supply that was phase locked to the supply driving the induction coil to prevent the two supplies from beating against each other and producing slowly varying changes

<sup>a)</sup>Electronic mail: jrwoodw@sandia.gov

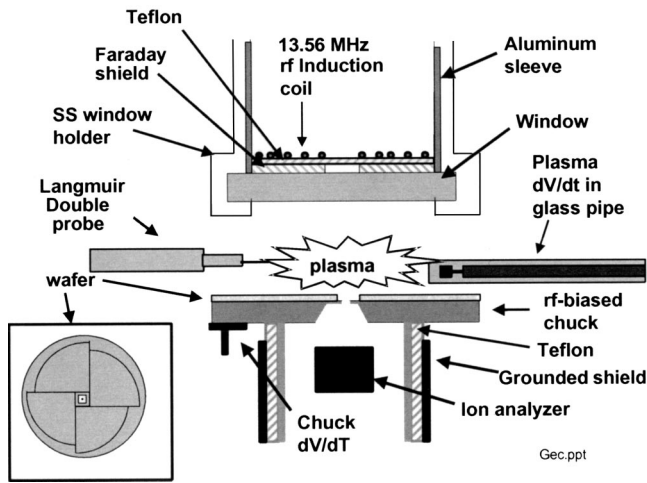


FIG. 1. Schematic of inductively coupled GEC Ref. Cell with rf biased wafer chuck. The ion analyzer samples through a  $5.5 \mu\text{m}$  pinhole on the chuck to collect the ions impacting the wafer. The inset shows a top view of the rf-biased chuck with the Si wafers on it.

in the IEDs. Capacitive-voltage probes were used to measure the rf components of both the plasma and chuck potentials. A double Langmuir probe<sup>39</sup> measured electron temperature and density at a point approximately 3 mm above the step.

It was necessary to cover most of the chuck surface with Si to prevent metal ions from sputtering off the stainless steel chuck and coating the fused silica rf entrance window when the chuck was biased. The inset in Fig. 1 shows a top view of our chuck with the wafer components on it. In the center of the figure is a 4.6 mm square, 300  $\mu\text{m}$  thick, undoped Si wafer with a 2.9 mm square hole in it. The nickel pinhole foil described below forms the bottom of this square hole. One inner wall of this 2.9 mm square functioned as our 300  $\mu\text{m}$  tall “straight wall” for these experiments. Previous work<sup>40</sup> suggests that the ion energy and angular distributions we measured in the center of a hole which was 2.9 mm square and only 300  $\mu\text{m}$  deep should be very close to the distributions on a flat surface. Four silicon “petals” formed of a quartered 6 in.-diam wafer were placed around the 4.6 mm square piece to cover the rest of the stainless steel chuck.

A pinhole at the bottom of the 2.9 mm square hole led to a separate vacuum system containing our gridded ion analyzer. We varied the position of the pinhole relative to the walls by gluing nominally identical walls down at different distances from “identical” pinholes with conductive epoxy. The 5.5  $\mu\text{m}$  diam pinholes were laser drilled in a nickel foil estimated by the manufacturer to be between 2 and 3  $\mu\text{m}$  thick.<sup>41</sup> The pinholes used were produced in a single run by the manufacturer, and appeared to have identical diameters to our experimental uncertainty of  $\pm 10\%$ .

## B. Gridded ion analyzer

Figure 2 shows a schematic of our gridded ion energy and angle analyzer that has been described in detail previously,<sup>36,42</sup> and only a brief description will be given

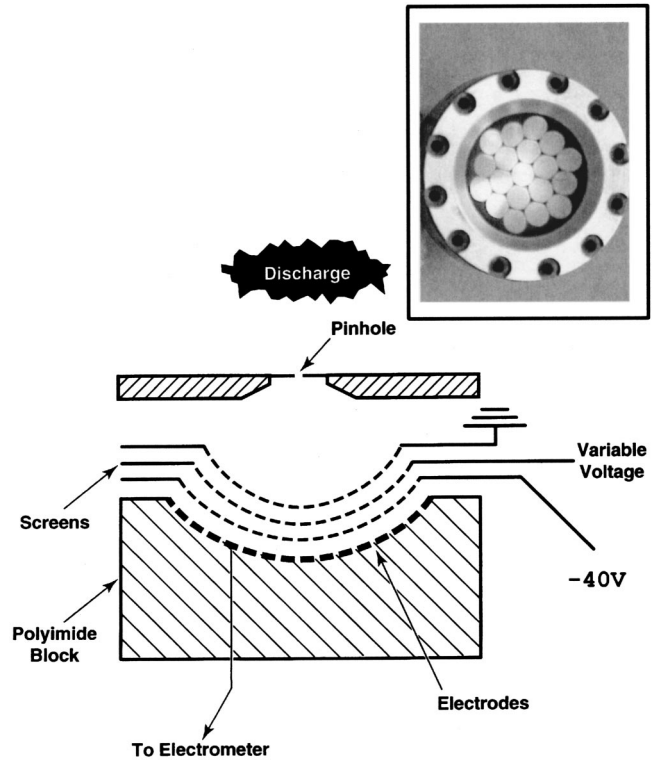


FIG. 2. Schematic of the three-screen gridded energy analyzer. The grids and the array of collection electrodes were formed into sections of nested hemispheres, all centered on the pinhole. This “nested hemisphere” format allowed us to measure ion angular distributions as well as ion energy distributions. The first grid was connected to the “local ground,” i.e., the wall of the rf-biased chuck, to create a field-free drift region between the pinhole and the analyzer. The inset shows a front view of the collector elements in our ion analyzer

here. The analyzer contains three screen grids and a series of 4.8 mm diam current collection electrodes. The stainless steel collection electrodes were stacked in a hexagonal close-packed array as shown in the inset in Fig. 2. The analyzer had three grids between the pinhole and the collection electrodes. Varying the voltage on the middle grid allowed us to sweep out the ion energy distribution. The grids and the surface of the bundle of electrodes were formed into sections of nested concentric spheres, all of which were centered on the pinhole. Hence, the surfaces of all the electrodes were on a spherical surface located 2.3 cm from the pinhole. Because the grids and collection electrodes were sections of spheres centered on the pinhole, ion trajectories were not affected by any external electric fields as the ions traveled from the pinhole to the electrodes. As a result, we could measure the ion angular distributions at the pinhole by comparing the current on the various electrodes. Based on previous work<sup>40</sup> we expect the sensitivity of this instrument to be independent of ion energy. The energy resolution of this detector ( $\Delta E/E$ ) is about 5%. Thus for 20 eV ions, we expect the detector resolution to be about 1 eV.

A point of great experimental importance is that the entire gridded analyzer was floated at the rf potential of the wafer chuck. In order to get the control voltages and collector currents into and out of the analyzer, we passed the signals

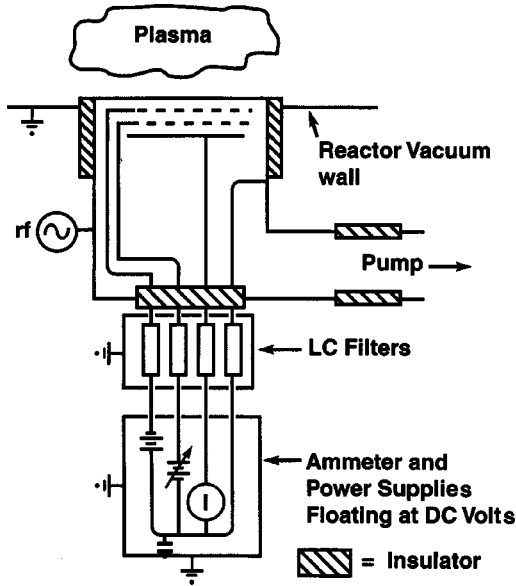


FIG. 3. Electrical schematic for ion analyzer. All signals in and out of the analyzer were passed through rf low pass filters which attenuated the 13.56 MHz chuck bias by  $\sim 50$  dB or more. This figure shows only one collector pin for simplicity. In reality there were 17 active collector pins and a total of 20 rf low-pass filters.

through rf low-pass filters<sup>43</sup> as shown in Fig. 3. After extraction from the rf biased area, the collector currents were passed through a low current switching system to a pico-ammeter. The switching system, the pico-ammeter, and the power supplies for the grid voltages were all controlled by a computer operating on LABVIEW software.

### III. SIMULATION

In this section, a two-dimensional ( $x$ - $y$ ) fluid/Monte Carlo simulation is reported, in an effort to predict the IEDs and IADs on an otherwise planar surface with a step (Fig. 4), in contact with a high density Ar plasma.

#### A. Fluid simulation

The compressible fluid equations for ions (species and momentum balances) coupled with Poisson's equation for the electric potential were employed.<sup>44,45</sup> Since the ion temperature is much lower than the electron temperature, the pressure force was ignored in the momentum balance equation. However, ion thermal effects were accounted for in the Monte Carlo simulation (see below). The viscous stress was also neglected in the ion momentum balance. The ion continuity and momentum balance equations would then read

$$\frac{\partial n_i}{\partial t} + \nabla \cdot (n_i \mathbf{u}) = 0, \quad (1)$$

$$\frac{\partial}{\partial t} (n_i \mathbf{u}) + \nabla \cdot (n_i \mathbf{u} \mathbf{u}) = -\frac{en_i}{m_i} \nabla \Phi - \nu_m n_i \mathbf{u}, \quad (2)$$

where  $n_i$ ,  $m_i$ ,  $\mathbf{u}$ , and  $\Phi$  are the ion density, ion mass, ion fluid velocity vector, and electric potential, respectively. The elementary charge is denoted by  $e$ , and  $\nu_m$  is the ion-neutral

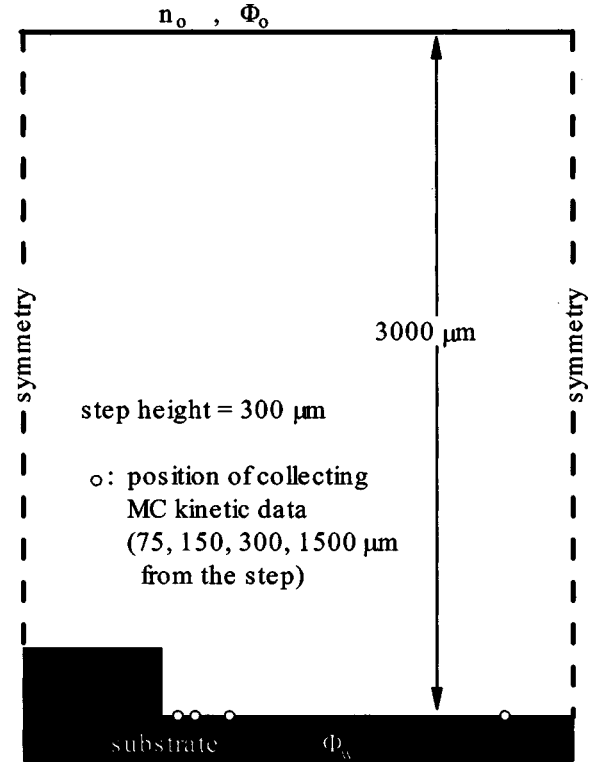


FIG. 4. Domain and boundary conditions used for simulations. The substrate step height is  $300 \mu\text{m}$ .

collision frequency, where ions could suffer elastic scattering or charge-exchange collisions. Poisson's equation reads

$$\nabla^2 \Phi = -\frac{e}{\epsilon_0} \left[ n_i - n_0 \exp\left(\frac{\Phi}{T_e}\right) \right], \quad (3)$$

where the potential  $\Phi$  is with respect to that of the upper boundary,  $\Phi_0$ ,  $\epsilon_0$  is the permittivity of free space, and  $n_0$  is the ion density at the upper boundary (Fig. 4). Electrons were assumed to be in Boltzmann equilibrium with the field, and the electron temperature  $T_e$  and background gas pressure and temperature (e.g., neutral density) were assumed to be spatially constant. A finite difference scheme based on the flux corrected transport method was implemented to solve the governing equations. This method is both transportive and conservative.<sup>46</sup> The equations were integrated in time by an explicit-Euler type method. The time step was chosen so that the Courant-Friedrichs-Lewy condition was satisfied. At each time step, Poisson's equation was solved iteratively to update the electric potential profile. The simulation evolved until a periodic steady state was reached.

The system employed in this study is shown in Fig. 4. An otherwise planar substrate with a  $300 \mu\text{m}$  tall step is located at the bottom of the domain. The potential was specified on the substrate  $\Phi_w$  and at the upper boundary  $\Phi_0$ , while both sides were symmetry planes ( $\nabla_n \Phi = 0$ ). At the upper boundary, the ion density  $n_0$  was specified but the ion flux (ion velocity) is unknown. When a flux was specified at the upper boundary of Fig. 4, spurious profiles of the ion density near the boundary were observed. The inlet ion fluid velocity

(having only a vertical component  $\nu_0$ ) was instead linearly extrapolated based on the values at the first two nodes

$$\nu_0 = 2\nu_1 - \nu_2. \quad (4)$$

This upstream condition has been used in compressible gas dynamics simulations before.<sup>46</sup> Equation (4) allows the inlet flux to develop as part of the solution. The specified electron temperature and ion density at the upper boundary set the value of the Debye length at that point. Note that the electron density was set equal to the ion density at the upper boundary, in accordance with the quasineutral plasma approximation. The plasma sheath (where charge neutrality breaks down) evolved self consistently, provided that the upper boundary of the domain was several times thicker than the sheath. The sheath thickness scales with the Debye length. Larger electron densities and lower electron temperatures (smaller Debye lengths) result in thinner sheaths (for a given sheath potential).

## B. Monte Carlo (MC) simulation

To begin the MC simulation, ions with the appropriate energy and angular distribution (see below) were launched at a plane near the sheath edge. The location of the sheath edge was defined as the position where the relative space charge is

$$\rho \equiv \frac{n_i - n_e}{n_i} = 0.01 \quad (5)$$

with the densities determined by the fluid simulation. The launch plane was such that the potential distribution was essentially 1D on that plane, i.e., the potential at that location was not perturbed by the presence of the step. Ions have a mean energy of the order of the electron temperature at the sheath edge.<sup>47</sup> In addition, ions have energy and angular distributions because of collisions with the background gas in the presheath. The mean directional energy of ions at the launch plane was first evaluated by

$$e_{\text{mean}} = \frac{1}{2}m_i(u^2 + v^2), \quad (6)$$

where  $u$  and  $v$  are  $x$  and  $y$  components of ion fluid velocity. (The ion fluid velocity at the launch location is essentially perpendicular, i.e.,  $u \approx 0$ .) The perpendicular (directional) energy of entering ions was then determined by

$$e_d = e_{\text{mean}} \cdot \varepsilon \quad (7)$$

where  $\varepsilon$  was picked from a Gaussian distribution

$$f(\varepsilon) = A_\varepsilon \exp\left(-\frac{1}{2}\left(\frac{\varepsilon - \mu}{\sigma_\varepsilon}\right)^2\right) \quad (8)$$

with  $\mu = 1.0$ ,  $\sigma_\varepsilon = 0.4247$ .

These values of  $\mu$  and  $\sigma_\varepsilon$  center the distribution at 1.0 and give it a full width at half maximum of 1.0. Using Eqs. (7) and (8) one can generate distribution functions similar to those produced by Riemann.<sup>47</sup> For the angular distribution of entering ions, the following formula was used.<sup>42</sup>

$$f(\theta) = A_\theta \exp\left(-\frac{1}{2}\left(\frac{\sin \theta}{\sigma_\theta}\right)^2\right) \quad (9)$$

with

$$\sigma_\theta = \sqrt{\frac{T_{i,\text{Tr}}}{2e_d}}, \quad (10)$$

where  $T_{i,\text{Tr}}$  is the transverse ion temperature. The angle picked from this distribution was shifted by  $\theta_{\text{mean}} \equiv \tan^{-1}(-u/v)$ , where  $u$  and  $v$  are again the ion's fluid velocity components at the launching position. Since ions are essentially perpendicular at this point,  $\theta_{\text{mean}} \approx 0$ . This way, the angular distribution of ions at the launch plane was centered at  $\theta_{\text{mean}}$  and had a spread of several degrees.

Once launched ions were accelerated by the spatially non-uniform and time-varying electric field determined by the fluid simulation. The three spatial coordinates and three velocity components ( $x, y, z, v_x, v_y, v_z$ ) were tracked in time by a fourth order Runge–Kutta method. During their transit through the sheath, ions can interact with the background neutral gas, i.e., they can suffer elastic scattering or charge-exchange collisions. A constant total cross section  $\sigma_t$  was used to evaluate the distance between collision events by the null collision method.<sup>48</sup> At the end of each free flight, the type of collision was determined according to the probability  $P_k = \sigma_k / \sigma_t$  for collision of type  $k$  ( $k$  can be elastic scattering, charge exchange, or null collision, i.e., no collision). The cross sections (in units of  $10^{-16} \text{ cm}^2$ ) for elastic scattering (SC) and charge-exchange (CX) collisions between  $\text{Ar}^+$  and Ar were obtained from Liebermann and Lichtenberg<sup>44</sup> and fit as follows:

$$\sigma_{\text{SC}} = 40.04(1.0 - 0.0563 \ln \varepsilon_{\text{kinetic}})^2, \quad (11)$$

$$\sigma_{\text{CX}} = 47.05(1.0 - 0.0557 \ln \varepsilon_{\text{kinetic}})^2, \quad (12)$$

where the ion kinetic energy  $\varepsilon_{\text{kinetic}}$  is in eV. Elastic scattering was treated as a hard sphere collision.<sup>49</sup> For charge exchange collisions, the (fast) ion and (slow) neutral switched identity (i.e., became fast neutral and slow ion, respectively) without altering their precollision velocity vector (resonant process). The resulting energetic (fast) neutrals could suffer elastic scattering further on, which was also treated as hard sphere collision. Fast neutrals, however, were primarily generated by neutralization of ions on the substrate (wall). Collision with the wall was assumed to result in specular reflection, with 100% neutralization of ions. Kinetic data for ions and fast neutrals were collected and recorded at four locations on the substrate, to facilitate comparison with experiments: 75, 150, 300, and 1500  $\mu\text{m}$  to the right of the step.

## IV. RESULTS

Table I lists plasma densities and electron densities measured with our double Langmuir probe for the Ar discharges. Table I also lists estimates of the Debye lengths and sheath sizes for these discharges. Sheath sizes are estimates for sheaths against a flat wafer.

A sample calculated electric potential profile is shown in Fig. 5. Parameter values were  $n_0 = 1.3 \times 10^{11} \text{ cm}^{-3}$ ,  $\Phi_0 = 17 \text{ V} + 8 \sin(\omega_{\text{RF}} t) \text{ V}$ ,  $\Phi_w = -16 \text{ V} + 19 \sin(\omega_{\text{RF}} t) \text{ V}$ , and the rf modulation frequency  $\omega_{\text{rf}}/2\pi$  was 13.56 MHz. The

TABLE I. Measured electron densities and temperatures along with estimates of Debye length and sheath thickness. The sheath edge was defined as the location where the relative net charge density is equal to 1% or  $(n_i - n_e)/n_i = 0.01$ . The sheath thickness shown are for cases without an rf bias on the wafer.

Pressure (mTorr)	Inductive coil power (W)	Electron temperature (eV)	Electron density ( $10^{11}/\text{cm}^3$ )	Debye length ( $\mu\text{m}$ )	Approximate sheath thickness ( $\mu\text{m}$ )
5	250	3.7	1.3	38	287
23	100	2.5	1.25	32	248
23	250	2.6	3.7	19	173
23	380	2.7	6.0	16	117

electron temperature  $T_e = 3.7$  eV, ion temperature  $T_i = 0.1$  eV, transverse ion temperature  $T_{i,Tr} = 0.1$  eV, gas temperature  $T_g = 0.05$  eV, and gas pressure  $P = 5$  mTorr, corresponding to the first row of Table I, but with an added 22 V peak-to-peak rf bias between the wafer and the plasma. The ion temperature was not measured, but was taken as a representative value.<sup>50</sup> Under these conditions, the sheath thickness was computed to be  $\sim 287$   $\mu\text{m}$ , which is comparable to the 300  $\mu\text{m}$  high step. As a result, the plasma “feels” the existence of the step and the sheath tries to wrap around the corner. The horizontal electric field (not shown) peaked at the upper corner of the step. Ions are expected to have quite different trajectories depending on their  $x$  coordinate above the step. Detailed theoretical results may be found in Kim and Economou.<sup>51</sup>

Figure 6 shows a plot of measured ion flux to the wafer versus distance from a 300  $\mu\text{m}$  tall wall for three different power levels in a 23 mTorr Ar discharge. Curves are shown with and without a  $\sim 20$  V<sub>pp</sub> rf bias between the wafer and the plasma. Several trends are evident from this figure. First, all the fluxes decrease sharply as our measurement point gets within 75  $\mu\text{m}$  of the wall. Second, at two of the induction

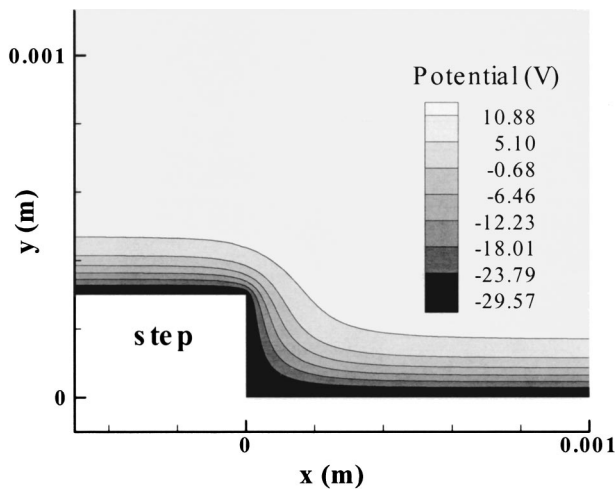


FIG. 5. Electric potential profile of argon plasma near step on rf-biased wafer in inductively driven GEC Ref. cell. Plasma density =  $1.3 \times 10^{11} \text{ cm}^{-3}$ . The data is shown for  $\tau_{rf} = 0.75$ , three quarters of the way through the rf cycle.

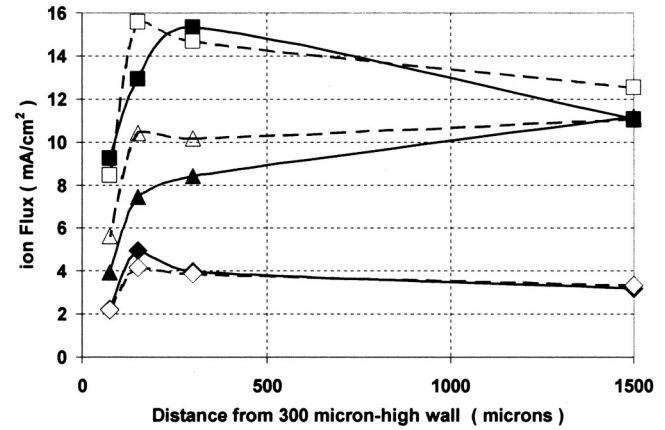


FIG. 6. Experimental ion fluxes vs position below a 300  $\mu\text{m}$  tall step on our rf biased wafer chuck. Data is shown at 23 mTorr total pressure for three different inductive powers: 100 W, lower curve with diamonds ( $\blacklozenge$ ); 250 W, middle curves with triangles ( $\blacktriangle$ ); and 380 W upper curves with squares ( $\blacksquare$ ). Data with no rf bias on the wafer is shown with filled data points and smooth curves. Data with  $\sim 20$  V peak-to-peak rf bias on the wafer is shown with hollow data points and dashed curves. The typical ion energy at this pressure was  $\sim 17$  eV with no rf bias. With rf bias, the ion energy distributions stretched from 15 to 35 eV.

coil power levels (100 and 380 W), the flux goes through a maximum as one moves away from the wall. Third, except for the data at 250 W, the presence of rf bias does not appear to significantly change the fluxes even though the presence of rf bias can significantly increase the calculated sheath thickness.

Figure 7 shows a plot of simulated ion flux to the wafer versus distance from the 300  $\mu\text{m}$  tall wall for the same pressure and inductive powers as Fig. 6, with no rf bias on the wafer. Adding a  $\sim 20$  V<sub>pp</sub> rf bias between the wafer and the plasma to the 250 W data did not significantly change the

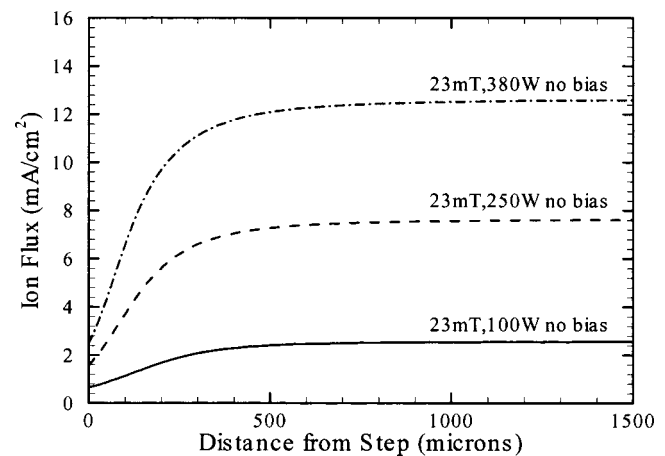


FIG. 7. Simulated ion fluxes vs position below the 300  $\mu\text{m}$  tall step on our rf biased wafer chuck. Simulations are shown at 23 mTorr total pressure for the same three inductive powers as Fig. 6, but without an rf bias on the wafer. Adding a  $\sim 20$  V peak-to-peak rf bias to the 250 W simulation did not significantly change the shape of the curve from the no-bias case. The simulations show the same trend of decrease in ion flux close to the wall as the data in Fig. 6, but do not replicate the maxima that are often seen in the experimental ion fluxes at about 200  $\mu\text{m}$  from the step.

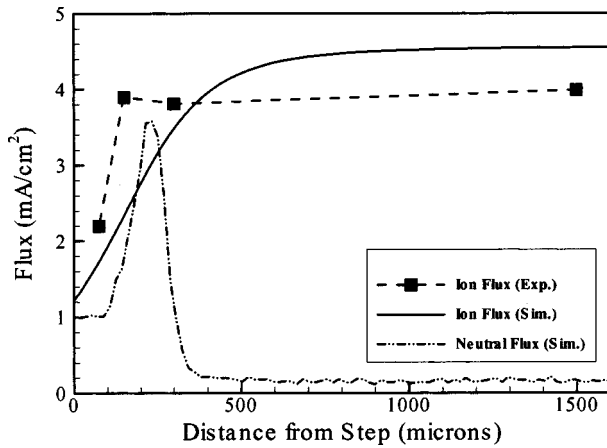


FIG. 8. Comparison of measured ion fluxes along with simulated ion and hot neutral fluxes close to the 300  $\mu\text{m}$  tall step in 5 mTorr, 250 W Ar discharges. The peak-to-peak rf bias voltage between the plasma and the chuck was 22 V for these measurements. The measured and predicted fluxes agree to about  $\sim 10\%$  far from the step and show similar trends as the sampling point approaches the step. The maximum in the hot neutral flux at  $\sim 250 \mu\text{m}$  is produced by ion collision with the sidewall and subsequent reflection of hot neutrals. Since the hot neutrals are also produced by charge exchange collisions in the gas phase, the neutral flux is not zero even at the location far away from the step.

simulated curve of flux versus position. The simulations show similar trends to the data in Fig. 6 in that the ion flux decreases close to the step, but the simulations do not show the maxima in ion fluxes that sometimes appear in the data.

Figure 8 shows a direct comparison between experiment and simulation for ion fluxes as our sampling point approaches the 300  $\mu\text{m}$  tall step. The calculated and measured ion fluxes far from the step are within about 10% of each other in this 5 mTorr Ar discharge with 250 W of induction power and 22 V rf bias. As the sampling point approaches the wall, experiment and simulation show the same trends, although the simulated ion flux begins decreasing farther from the step than the experimental data does. This figure also shows simulated hot neutral fluxes versus position. The peak in the hot neutrals at about  $\sim 250 \mu\text{m}$  is caused by ions striking the sidewall and being reflected as hot neutrals.

Figure 9 shows measured (a) and calculated (b) ion energy distributions versus distance from the 300  $\mu\text{m}$  tall wall for 5 mTorr discharges with 250 W of induction drive power. Both the measurements and the model show the expected double-peaked IEDs that narrow as the sampling point approaches the 300  $\mu\text{m}$  tall wall. The data, however, show IEDs with a  $\sim 19$  V separation between peaks whereas the calculated IEDs have only a  $\sim 16$  V separation between peaks. Figures 10(a) and 10(b) show a similar theory-to-experiment comparison for data taken in a 23 mTorr Ar discharge with 250 W of induction coil power. Again, theory and experiment show the same trends, although the theoretical IED curves are narrower than the data.

Figure 11 displays ion angular distributions in 5 mTorr Ar discharges as a function of distance between the sampling aperture and the wall. These discharges were driven by 250 W induction power. The peak-to-peak rf bias voltage be-

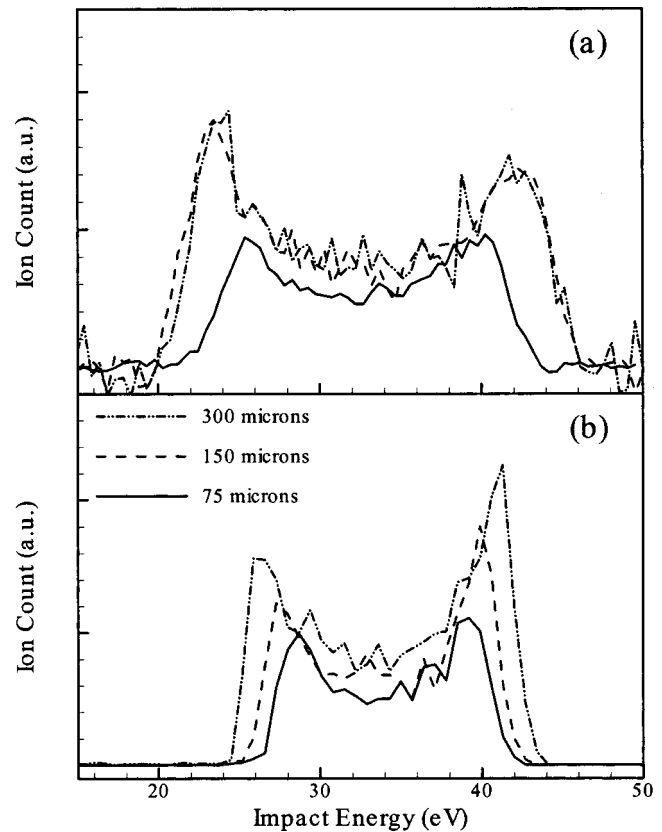


FIG. 9. Comparison of ion energy distributions versus position below a 300  $\mu\text{m}$  tall step on our rf-biased wafer chuck in 5 mTorr Ar discharges with 250 W of rf power to the induction coil: (a) experimental measurements and (b) model calculations. The rf bias between the chuck and plasma was fixed at  $\sim 22$  V for all of this data, but the ion energy distributions still narrow as the sampling point approached the step.

tween the plasma and chuck varied from 21 to 26 V for these data. These “target plots” display ion flux (in nA) on each of the elements in the hexagonal-close-packed array on our collector (refer to Fig. 3 for collector layout). The plotting routine has smoothed the transitions between signal levels on adjacent pins to improve the legibility of the figure. The concentric circles represent the solid angles defined by cones whose apex is at the sampling hole and which sweep out points which are  $\sim 6.4^\circ$ ,  $12.9^\circ$ , and  $19^\circ$  off the normal to a flat wafer surface. The sampling hole remained centered over the central pin on our detector for all of these experiments as the 300  $\mu\text{m}$  tall step was moved closer to the sampling hole. The wall is shown as a rectangular block. The beam’s angular distribution moves  $\sim 19^\circ$  off axis toward the wall as the sampling point moves in toward the step, starting at 1500  $\mu\text{m}$  and moving in to 75  $\mu\text{m}$  from the wall. In some cases the distributions also spread noticeably, spilling over onto two or more detector pins. Finally, the fluxes decrease as the distribution moves close to the wall, reflecting the trends seen Figs. 6–8.

The experimental ion angular data shows intensity versus angle off the pinhole axis  $\theta$  and azimuthal angle around the pinhole  $\varphi$ , whereas the simulations show just intensity versus angle off the pinhole axis  $\theta$ . To compare the data to the

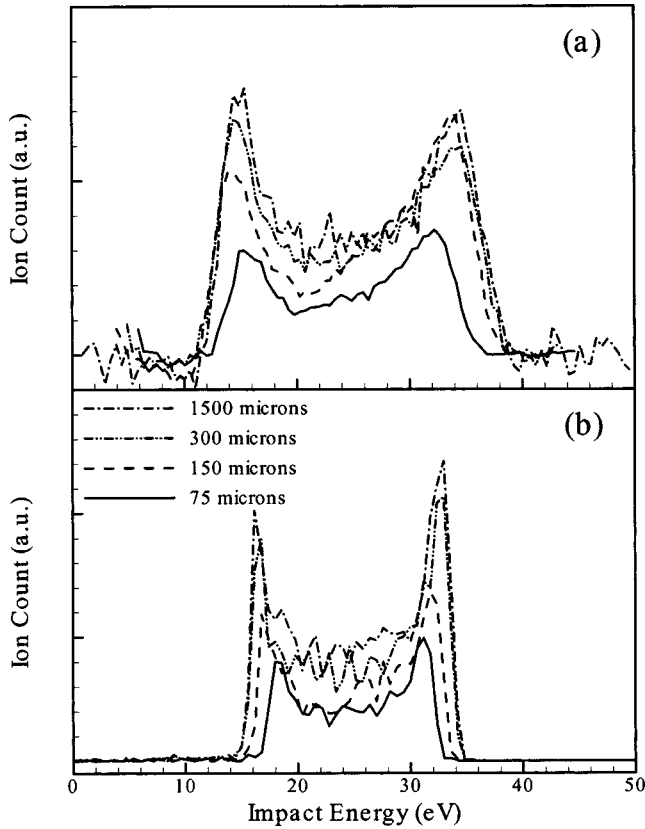


FIG. 10. Comparison of ion energy distributions vs position below a 300  $\mu\text{m}$  tall step on our rf-biased wafer chuck in 23 mTorr Ar discharges with 250 W of rf power to the induction coil: (a) experimental measurements and (b) model calculations. The peak-to-peak rf bias voltage between the chuck and plasma was fixed at 19 V for these measurements. Although the plasma sheath is considerably narrower than in Fig. 9, the trends in the two figures are similar.

simulations, therefore, we took 1D “cuts” through the type of experimental data shown in Fig 11, (eliminating  $\varphi$ ), which yielded data that could be compared directly to the simulations.

Figures 12 and 13 show these approximations to the ion angular data and compare this data with model calculations. Again, in the experimental data, transitions between different signal levels on adjacent pins have been smoothed slightly to improve the legibility of the figure. While the experimental data have very crude angular resolution (each pin is  $12^\circ$  wide), the trends of the beam moving off axis toward the wall are clearly the same. Also, note that to within the accuracy of the experimental data, the angular displacements of the beam from the axis agree in the experiment and model.

## V. DISCUSSION

The decrease in ion fluxes near the step can be understood by looking at the calculated equipotentials in Fig. 5. Far from the step, where the equipotentials are flat, ions that are  $\sim 50 \mu\text{m}$  apart when they begin crossing the sheath will still, on average, be  $50 \mu\text{m}$  apart when they strike the wafer. The convex curvature of the equipotentials below the step however, means that ions that are  $\sim 50 \mu\text{m}$  apart when they start

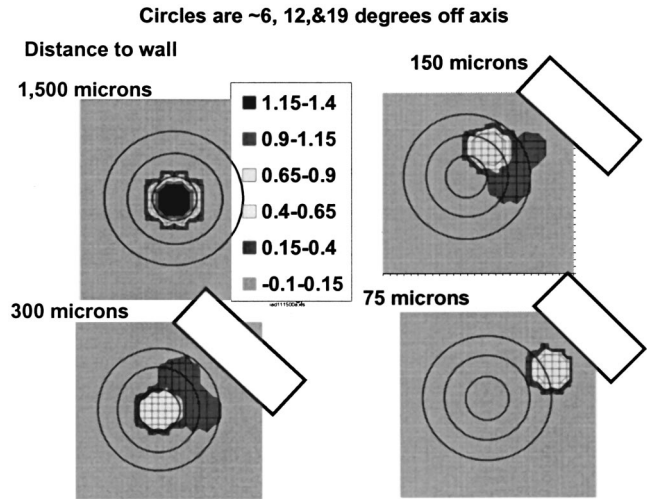


FIG. 11. Surface plots of ion angular distributions versus position below a 300  $\mu\text{m}$  tall step for 5 mTorr Ar discharges with 250 W induction drive and rf bias levels between 21 and 26 V peak-to-peak between plasma and chuck. The plots show ion flux in nA on each of the pins on our 19 pin detector array as the sampling aperture moves toward the step. The box indicates the direction of the step. The concentric circles represent the solid angles defined by cones whose apex is at the sampling hole and which sweep out points which are  $\sim 6.4^\circ$ ,  $12.9^\circ$ , and  $19^\circ$  off the normal to a flat wafer surface. The sampling hole remained centered over the central pin on our detector for all of these experiments as the 300  $\mu\text{m}$  tall step was moved closer to the sampling hole. The angular distribution of the beam broadens and moves toward the step as the sampling aperture approaches the step. Transitions between different signal levels on adjacent pins have been smoothed slightly to improve legibility of the figure.

across the sheath close to the step will be spread out over a relatively large area (e.g.,  $\sim 200 \mu\text{m}$ ) when they strike the wafer, lowering the effective flux on the wafer 75  $\mu\text{m}$  from the step.

The curvature of the equipotentials over the step also means that the electric fields will deflect the angular distribution of the ions toward the step as seen in both the theory and the data (Figs. 11–13). The simulation suggests that many ions will strike the vertical wall of the step and reflect as hot neutrals, striking the horizontal surface near the foot of the step. In fact, the flux of hot neutrals near the foot of the step is predicted to be comparable to the ion flux (Fig. 8). Since fast neutrals can have a significant impact on etching, it is important to include these hot neutrals in feature evolution simulations. Some of the ions striking the vertical wall may have been reflected as ions. If so, these ions apparently had their trajectories curved back toward the base of the step by the bowed  $E$  fields near the step since we saw no ions close to the step with trajectories that aimed away from the step (Fig. 11). These ions that had been reflected off the vertical wall as ions may have contributed to the maxima in the ion fluxes we observed at about 200  $\mu\text{m}$  from the base of the wall.

The experimental data and the model calculations both show a narrowing of the width of the double-peaked ion energy distributions as the sampling aperture approaches the 300  $\mu\text{m}$  tall step. This narrowing occurs because of the increase in sheath thickness as the sampling point approaches

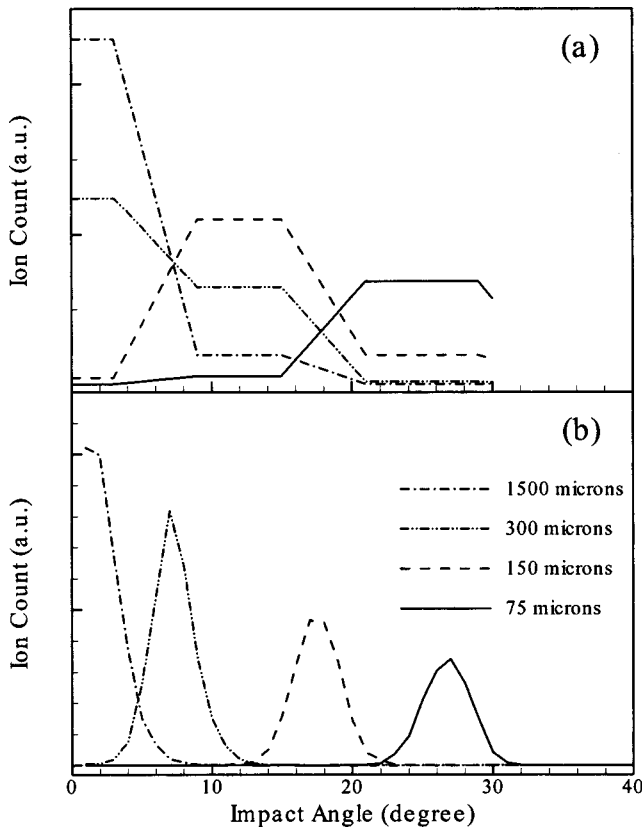


FIG. 12. 2D measurements (a) and calculations (b) of ion angular distributions for 5 mTorr Ar, discharge with 250 W induction drive and  $\sim 22 V_{pp}$  rf bias on chuck. In the experimental data, transitions between different signal levels on adjacent pins have been smoothed slightly to make the figure more legible. The calculations display the detailed angular distribution of the ions at each distance from the wall.

the step. On a flat surface, the ions cross the sheath in a smaller fraction of a rf period and therefore see more of an instantaneous value of the rf bias potential. Under these conditions, the width of the double-peaked IED is close to the peak-to-peak voltage difference between the bulk plasma and the chuck. Ions take a significant fraction of a rf period, however, to cross the relatively larger sheath below the step. Thus, the ions tend to see more of a “time-averaged” rf potential instead of an instantaneous value. This time averaging compresses the IED, reducing the distance between the high- and low-energy peaks.

The experimental IEDs are consistently slightly broader than the widths obtained from the calculations. We suspect this discrepancy can be traced to the limitations of our plasma density measurements. Previous work comparing Langmuir probe data to microwave interferometer measurements<sup>38</sup> demonstrates that the presence of a probe can depress the local plasma density by a factor of 2. Arbitrarily increasing the plasma densities used as inputs to the calculations by a factor of 2 removes most of the discrepancy between the modeled and experimental IED widths.

We have previously reported<sup>32</sup> that space-charge-induced beam broadening inside our gridded analyzer can broaden the angular distributions we measure. We do see some indi-

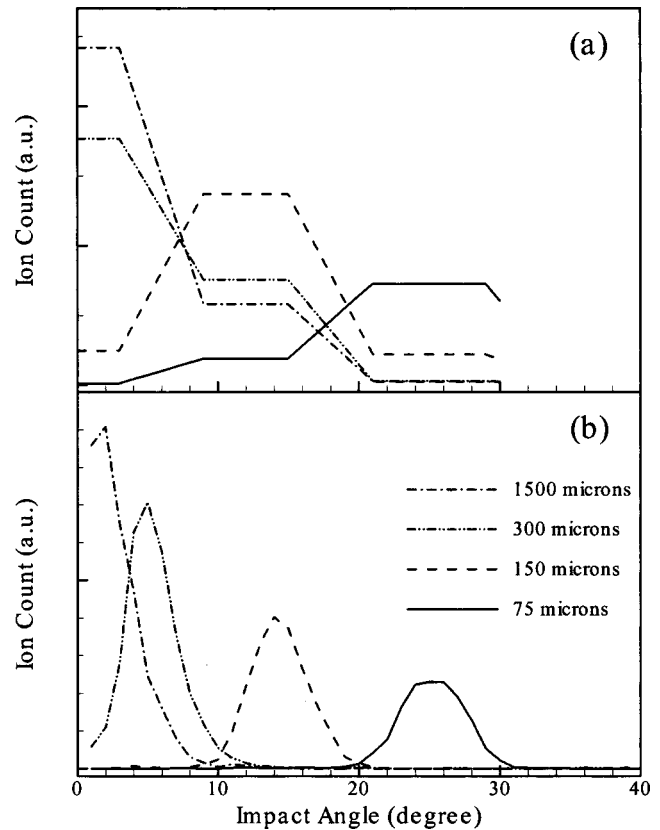


FIG. 13. 2D measurements (a) and calculations (b) of ion angular distributions for 23 mTorr Ar, discharge with 250 W induction drive and  $\sim 21 V_{pp}$  rf bias on chuck as the sampling point moves toward the 300  $\mu\text{m}$  tall step.

cations of beam broadening in these experiments. The non-zero “foot” on the first curve in Fig. 12(a) between  $\sim 8^\circ$  and  $\sim 16^\circ$  (this is the data taken 1500  $\mu\text{m}$  from the wall) is probably due entirely to beam broadening inside the analyzer. These effects, however, do not significantly alter the ion fluxes, energy distributions, or mid points of the ion angular distributions we report in this work.

Our experiments were carried out using argon gas since use of real etching gases would rapidly erode both our sampling aperture foils and the 300  $\mu\text{m}$  tall step. In true etching gas discharges, we would expect several changes. The attaching gases in the mixtures would yield many negative ions and a lower electron density, lowering plasma potentials. The negative ions would be repelled by the sheath fields, so it should be adequate to simulate only positive ion and electron propagation in the sheath fields. In etching mixtures, there will typically be a number of ion species of different masses present at the edge of the sheath. Each of these ion species will contribute to the sheath dynamics differently in accordance with their different transit times. To first order, we would expect the simulation results to be a linear combination of the results of a number of single ion cases.

## VI. SUMMARY

We have compared model calculations and experimental data of ion distributions close to 300  $\mu\text{m}$  tall “steps” on

rf-biased silicon wafers in high-density argon plasmas. Simulations have successfully predicted most of the trends seen in these experiments. As our sampling point approaches the step from below, the ion fluxes decrease, the ion angular distributions move away from vertical toward the step, and the width of the double-peaked ion energy distributions decrease. As seen in the simulations, all of these effects can be accounted for by curvature of the plasma sheath around the 300  $\mu\text{m}$  tall step. The simulation suggests that many ions will strike the vertical wall of the step and reflect as hot neutrals, striking the horizontal surface near the foot of the step. In fact, the flux of hot neutrals near the foot of the step is predicted to be comparable to the ion flux. Thus hot neutrals can make important contributions to etching. Local maxima in the ion fluxes seen at about 200  $\mu\text{m}$  from the step are not predicted by the simulations and may be partly due to ions being reflected off the vertical wall of the step as ions.

## ACKNOWLEDGMENTS

The authors wish to acknowledge many helpful discussions with Dr. G. A. Hebner and Dr. M. E. Riley at Sandia Laboratories. Financial support was provided by Sandia National Laboratories, NSF Contract No. CTS-0072854, and the NSF-supported MRSEC at the University of Houston. Sandia is a multiprogram laboratory operated by Sandia Corporation, a Lockheed Martin Company, for the United States Department of Energy under Contract No. DE-ACO4-94AL85000.

- <sup>1</sup>J. R. Wendt, T. W. Krygowski, G. A. Vawter, O. Blum, W. C. Sweatt, M. E. Warren, and D. Reyes, *J. Vac. Sci. Technol. B* **18**, 3608 (2000).
- <sup>2</sup>P. G. Datskos, S. Rajic, M. J. Sepaniak, N. Lavrik, C. A. Tipple, L. R. Senesac, and I. Datskou, *J. Vac. Sci. Technol. B* **19**, 1173 (2001).
- <sup>3</sup>M. Gad-el-Hak, *MEMS Handbook* (Chemical Rubber Corp., Boca Raton, FL, 2001).
- <sup>4</sup>E. Kawamura, V. Vahedi, M. A. Lieberman, and C. K. Birdsall, *Plasma Sources Sci. Technol.* **8**, R45 (1999).
- <sup>5</sup>M. A. Sobolewski, *Phys. Rev. E* **62**, 8540 (2000).
- <sup>6</sup>D. Bose, T. R. Govindan, and M. Meyyappan, *J. Appl. Phys.* **87**, 7176 (2000).
- <sup>7</sup>E. A. Edelberg and E. S. Aydil, *J. Appl. Phys.* **86**, 4799 (1999).
- <sup>8</sup>P. A. Miller and M. E. Riley, *J. Appl. Phys.* **82**, 3689 (1997).
- <sup>9</sup>R. J. Hoekstra, M. J. Grapperhaus, and M. J. Kushner, *J. Vac. Sci. Technol. A* **15**, 1913 (1997).
- <sup>10</sup>E. Meeks, P. Ho, A. Tingand, and R. J. Buss, *J. Vac. Sci. Technol. A* **16**, 2227 (1998).
- <sup>11</sup>J. Johannes, T. Bartel, G. Hebner, J. Woodworth, and D. Economou, *J. Electrochem. Soc.* **144**, 2448 (1997).
- <sup>12</sup>T. Kinoshita, M. Hane, and J. P. McVittie, *J. Vac. Sci. Technol. B* **14**, 560 (1996).
- <sup>13</sup>G. S. Hwang and K. P. Giapis, *J. Vac. Sci. Technol. B* **15**, 70 (1997).
- <sup>14</sup>A. N. Goyette, Y. Wang, M. Misakian, and J. K. Olthoff, *J. Vac. Sci. Technol. A* **18**, 2785 (2000).
- <sup>15</sup>C. A. Nichols, J. R. Woodworth, and T. W. Hamilton, *J. Vac. Sci. Technol. A* **16**, 3389 (1998).
- <sup>16</sup>U. Kortshagen and M. Zethoff, *Plasma Sources Sci. Technol.* **4**, 541 (1995).
- <sup>17</sup>J. R. Woodworth, M. E. Riley, P. A. Miller, C. A. Nichols, and T. W. Hamilton, *J. Vac. Sci. Technol. A* **15**, 3015 (1997).
- <sup>18</sup>J. Hopwood, *Appl. Phys. Lett.* **62**, 940 (1993).
- <sup>19</sup>E. S. Aydil, B. O. M. Quiniou, J. T. C. Lee, J. A. Gregus, and R. A. Gottscho, *Mater. Sci. Semicond. Process* **1**, 75 (1998).
- <sup>20</sup>K. Kohler, J. W. Coburn, D. E. Horne, E. Kay, and J. H. Keller, *J. Appl. Phys.* **57**, 59 (1985).
- <sup>21</sup>J. Hopwood, *Appl. Phys. Lett.* **62**, 940 (1993).
- <sup>22</sup>M. G. Blain, J. E. Stevens, J. R. Woodworth, and C. E. Nichols, *Proceedings of the 9th Conference on Plasma Dynamics and Lasers*, Albuquerque, NM, June 1998.
- <sup>23</sup>J. Janes, *J. Vac. Sci. Technol. A* **12**, 97 (1994).
- <sup>24</sup>A. D. Kuppers and H. J. Hopman, *J. Appl. Phys.* **67**, 1229 (1990).
- <sup>25</sup>F. Becker, I. W. Rangelow, and R. Kassing, *J. Appl. Phys.* **89**, 56 (1996).
- <sup>26</sup>M. Zeuner and H. Neumann, *J. Appl. Phys.* **81**, 2985 (1997).
- <sup>27</sup>A. Mannenschiijn, E. van der Drift, G. C. A. M. Janssen, and S. Radelaar, *J. Appl. Phys.* **69**, 7996 (1991).
- <sup>28</sup>N. Mizutani and T. Hayashi, *J. Vac. Sci. Technol. A* **19**, 1298 (2001).
- <sup>29</sup>P. K. Loewenhardt, H. Hanawa, D. X. Ma, P. Salzman, K. Chuc, A. Sato, V. Todorov, and G. Z. Yin, *Proc.-Electrochem. Soc.* **96**, 234 (1996).
- <sup>30</sup>J. Trow, *Bull. Am. Phys. Soc.* **39**, 1488 (1994).
- <sup>31</sup>Y. Hikosaka, H. Hayashi, M. Sekine, H. Tsuboi, M. Endo, and N. Mizutani, *Jpn. J. Appl. Phys., Part 1* **38**, 4465 (1999).
- <sup>32</sup>J. R. Woodworth, I. C. Abraham, M. E. Riley, P. A. Miller, T. W. Hamilton, B. P. Aragon, R. J. Shul, and C. G. Willison, *J. Vac. Sci. Technol. A* **20**, 873 (2002).
- <sup>33</sup>E. A. Edelberg, A. Perry, N. Benjamin, and E. S. Aydil, *J. Vac. Sci. Technol. A* **17**, 506 (1999).
- <sup>34</sup>I. C. Abraham, J. R. Woodworth, M. E. Riley, P. A. Miller, T. W. Hamilton, and B. P. Aragon, *J. Vac. Sci. Technol. A* **20** (in press).
- <sup>35</sup>J. R. Woodworth, B. P. Aragon, and T. W. Hamilton, *Appl. Phys. Lett.* **70**, 1947 (1997).
- <sup>36</sup>J. R. Woodworth, P. A. Miller, R. J. Shul, I. C. Abraham, B. P. Aragon, T. W. Hamilton, and C. G. Willison, *J. Appl. Phys.* **92**, 716 (2002).
- <sup>37</sup>P. J. Hargis *et al.*, *Rev. Sci. Instrum.* **65**, 140 (1994).
- <sup>38</sup>P. A. Miller, G. A. Hebner, K. E. Greenberg, P. D. Pochan, and B. P. Aragon, *J. Res. Natl. Inst. Stand. Technol.* **100**, 427 (1995).
- <sup>39</sup>R. J. Shul and S. J. Pearton, *Handbook of Advanced Plasma Processing Techniques* (Springer, New York, 2000), p. 148.
- <sup>40</sup>J. R. Woodworth, M. E. Riley, P. A. Miller, G. A. Hebner, and T. W. Hamilton, *J. Appl. Phys.* **81**, 5950 (1997).
- <sup>41</sup>National Aperture, 26 Keewaydin Drive, Salem, New Hampshire 03079, (603) 893-7393.
- <sup>42</sup>J. R. Woodworth, M. E. Riley, D. C. Meister, B. P. Aragon, M. S. Le, and H. H. Sawin, *J. Appl. Phys.* **80**, 1304 (1996).
- <sup>43</sup>K & L Microwave Inc., 22540 Northwood Dr., Salisbury, MD 21801.
- <sup>44</sup>M. A. Lieberman and A. J. Lichtenberg, *Principles of Plasma Discharges and Material Processing* (Wiley, New York, 1994), p. 73.
- <sup>45</sup>M. Hong and G. A. Emmert, *J. Vac. Sci. Technol. B* **12**, 889 (1994).
- <sup>46</sup>P. J. Roache, *Fundamentals of Computational Fluid Dynamics* (Hermosa, Albuquerque, NM, 1998).
- <sup>47</sup>K.-U. Riemann, *Phys. Fluids* **24**, 2163 (1981).
- <sup>48</sup>J. P. Boeuf and E. Marode, *J. Phys. D* **15**, 2169 (1982).
- <sup>49</sup>J. O. Hirschfelder, C. F. Curtiss, and R. B. Bird, *Molecular Theory of Gases and Liquids* (Wiley, New York, 1954).
- <sup>50</sup>G. A. Hebner, C. B. Fleddermann, and P. A. Miller, *J. Vac. Sci. Technol. A* **15**, 2698 (1997).
- <sup>51</sup>D. Kim and D. J. Economou, *IEEE Trans. Plasma Sci.* (accepted for publication).